PAYLOAD CHARACTERIZATION OF AN AIRBORNE PUSH-BROOM HYPERSPECTRAL IMAGER

Micherene Clauzette Lofamia[1], Mara Alain Maestro, Ralph Aaron Aguinaldo, Andrew Rafael Bañas,
and Maricor Soriano
National Institute of Physics, University of the Philippines Diliman, 1101 Quezon City, Philippines,
[1]Email: mplofamia@up.edu.ph

KEY WORDS: push-broom, hyperspectral, characterization

ABSTRACT: An airborne hyperspectral imaging sensor can capture data containing 2D spatial information and spectrum in the third dimension. A push-broom hyperspectral imaging system can obtain the 3D information by capturing the dispersed spectral components from a single line slit of spatial information, then scanning perpendicular to the slit to obtain the complete 2D spatial information. This study aims to characterize different properties of the in-house developed airborne push-broom hyperspectral imaging sensor with commercial off-the-shelf (COTS) components. The payload system has undergone sensor characterization by determining and calculating the dark current bias, linearity, photon transfer curve, and flat-field of the detector. Moreover, the image quality is further examined by measuring the payload system's modulation transfer function (MTF). Lastly, the effect of the imaging spectrometer on spectral, spatial, and intensity components was investigated using simulations and actual tests of the payload prototypes with 50 and 80-micrometer slits.

1. INTRODUCTION

Hyperspectral imaging has been of great interest for the past few decades due to its ability to provide detailed and continuous spectral information of a 2-dimensional target scene. Pushbroom hyperspectral imager collects this 3D hyperspectral data by capturing the dispersed spectral components from a single line and scanning perpendicularly to obtain the complete spatial information (Aasen et al., 2018; Stuart et al., 2019). Miniaturized versions of this instrument enable its utilization on airborne platforms, such as drones, which can readily provide high resolution and quality data on-demand for local or regional use (Aasen et al., 2018; Stuart et al., 2019; Hruska et al., 2012). With these advantages, airborne push-broom hyperspectral imagers are widely used in various applications such as in agriculture and forest monitoring (Adão et al., 2017).

Data measurements by airborne push-broom hyperspectral imagers, like any other sensors, are affected by factors intrinsic to the system (Barreto et al., 2019). This includes the optoelectronic performance of the camera, such as the sensor's sensitivity, dark current, noise, and flatness of field (Pagnutti et al., 2017). Besides the camera sensor's characteristics, analyzing the effects of lens and imaging spectrometers on data quality is also necessary to understand the system's capabilities. Characterization of these properties, which aids the calibration process, is necessary for the development of the airborne push-broom hyperspectral imager and its field deployment operations planning. Moreover, the characterization would be necessary for corrections before radiometric calibrations to produce an accurate and repeatable measurement for mission applications (Barreto et al., 2019).

This study aims to characterize different properties of an in-house developed airborne push-broom hyperspectral imaging sensor with commercial off-the-shelf (COTS) components to acquire high-quality data for its agricultural missions.

2. OPTICAL ASSEMBLY

The main components of the push-broom hyperspectral imaging sensor are shown in Figure 1. After the front lens images the target scene, the entrance slit of the imaging spectrometer crops out a single line then disperse the image into its wavelength components. A USB camera sensor captures this 2D image containing the spectral and spatial axis.
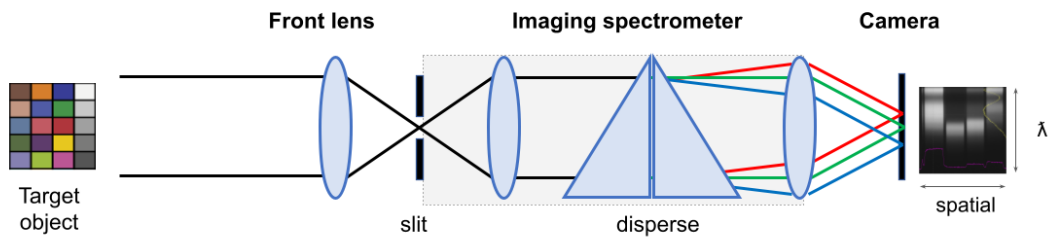
Figure 1. Payload optical assembly of the in-house developed airborne push-broom hyperspectral imaging sensor.

Commercially available components were utilized and assembled to complete the optical payload system. The 12mm ruggedized lens was acquired from Edmund Optics (#35-156) for its shock tolerance ideal for drone campaigns and its cost-effectivity. The SPECIM Imspector V10 was used as the imaging spectrometer. This includes the entrance slit to take a single line of spatial information and the prism-grating-prism (PGP) component to disperse the wavelength components. PGP is a dispersing element with high diffraction efficiency and a straight optical axis optimal for miniaturized hyperspectral imagers (Aikio, 2001). Lastly, the camera used is FLIR's (PtGrey) FL3-U3-13Y3M-C – a monochromatic CMOS with an available software development kit for programming an image capture software suitable for field deployment operations.

3. PAYLOAD CHARACTERIZATION

In this study, the intrinsic properties of the camera, imaging spectrometer, and lens were characterized. This section is divided into three parts: (1) sensor characterization for illustrating the optoelectronic characteristics of the USB camera, (2) image quality analysis for the calculation of the resolution limit, and (3) imaging spectrometer analysis for the effect of the slit and PGP on intensity, spectral and spatial components.

3.1 Sensor Characterization

In this section, the intrinsic properties of the camera sensor are discussed. This includes the dark current assessment, camera linearity, image noise assessment, and flat fielding.

Dark current assessment: To investigate the dark noise bias of the camera sensor, 20 dark frame captures were obtained for varying camera exposure time and gain settings. The linearity of the camera measurements was analyzed. As seen in Figure 2, the dark current is independent of exposure time, as expected. On the other hand, the mean camera digital number (DN) values were found to be highly linear with the gain factor. It is also evident that the variability of the DN values increases as gain increases. Moreover, it is important to note that the dark current is known to be dependent on temperature (Pagnutti et al., 2017; Adão et al., 2017). Thus, for the image corrections, the dark current correction image must be measured at the same camera temperature as the data to be corrected.
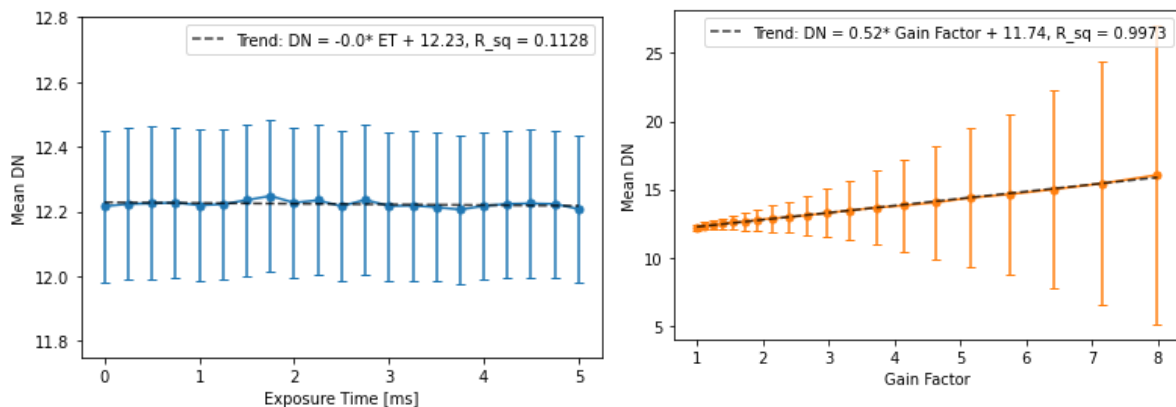

Figure 2. Dark current values variability with respect to exposure time (left) and gain settings (right).

Camera linearity: The camera linearity with respect to exposure time and gain settings was also evaluated by imaging an integrating sphere using the bare USB camera. To investigate the exposure time linearity, 20 bright frames were captured at a 0dB gain for each exposure time. As shown in Figure 3, the mean DN value measurements were found to be linear with respect to exposure time settings. On the other hand, the gain linearity was evaluated by also obtaining 20 bright frames for each gain setting at 5ms exposure time. It is evident that the camera values are also linear with respect to gain. It is noted that for both linearity, there is a deviation from the linear trends and a decrease in variance for high mean DN values due to saturation of some pixels.
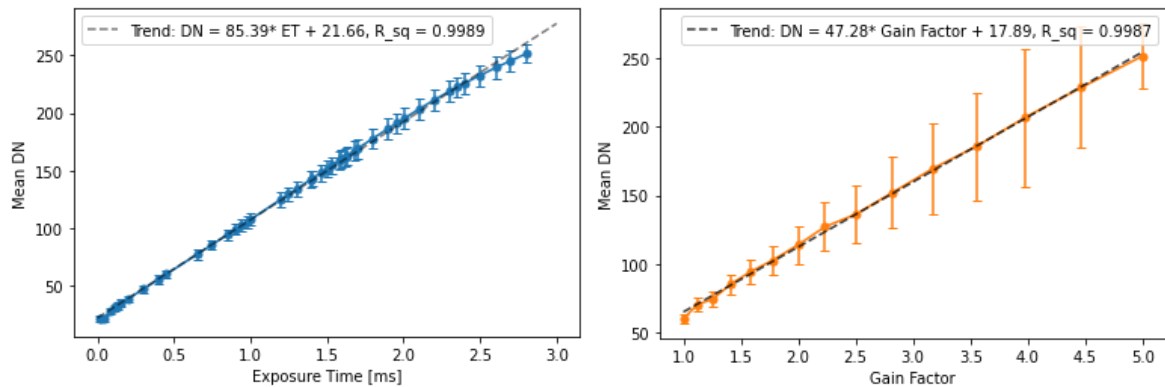

Figure 3. Camera linearity with exposure time (left) and gain settings (right).

Noise characterization : To characterize the inherent noise of the bare USB Camera, an experiment to graph the photon transfer curve was conducted. The sensor was made to capture the integrating sphere at constant illumination and gain across different exposure times (Janesick, 2007). A total of 59 exposure time values ranging from 0.010 to 2.803 ms are used. For each set of parameters, 21 captures were taken and were averaged. The mean pixel value and the image variance were each computed. The photon transfer curve describing the noises in four regimes (fixed pattern, read, fixed pattern, full regime) is yielded from these data. A better noise quantification is done by subtracting consecutive captures of the same experiment parameter, thus, removing the fixed pattern noise across the data (Janesick, 2007). The resulting noise is shown in Figure 4.
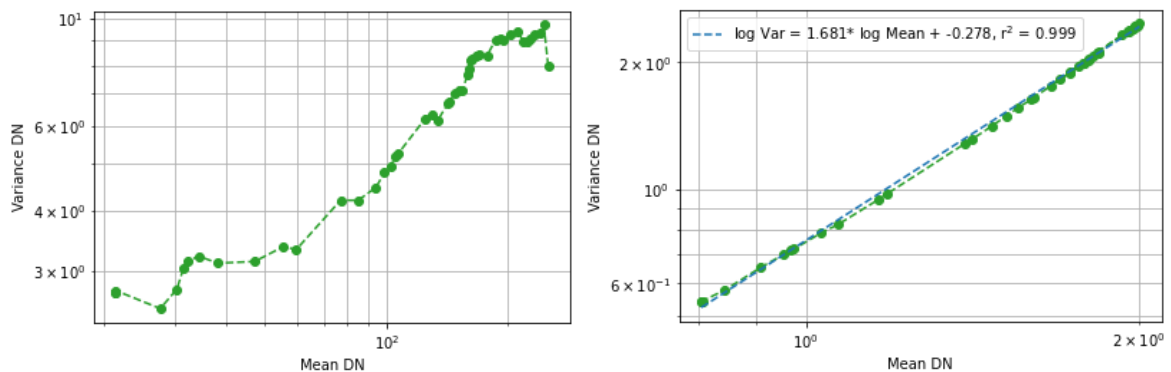

Figure 4. Photon transfer curve (left) and PTC with fixed pattern noise removal (right).

Flatness of field: Given the components of the optical assembly, there are three possible sources of non-uniformity affecting the supposed flatness of field - the USB camera, the imaging spectrometer, and the lens. Two experiments were carried out to characterize these where the bare USB camera and the whole optical assembly captured a different set of flat, bright images (integrating sphere image).

A simple normalization of the dark corrected flat image to its average value was done to characterize the non-uniformity of the CMOS sensor using the equation

$$\square_I \ = \ (\square_I - \square) \,/\, \underline{(\square_I - \square)}_{\square,\square} \tag{1}$$

where $\square_1$ is the non-uniformity correction due to CMOS sensor, $\square_1$ is the bare USB camera flat image and $\square$ is the dark noise correction image. Upon inspection of these images, the CMOS sensor itself does not exhibit a flat field despite any lens.

Moreover, the non-uniformity caused by the imaging spectrometer and the stock lens was collectively characterized similarly with the bare CMOS sensor non-uniformity characterization. Unlike that of the USB camera, the non-uniformity caused by these two components are yielded along the spatial axis alone. The normalized dark and CMOS flat-field corrected with respect to its average value along the spatial axis was obtained using the equation

$$\square_2 = [(\square_2 - \square) \div \square_1] / \underline{[(\square_2 - \square) \div \square_1]}_\square \qquad (2)$$

where $\square_2$ is the non-uniformity correction due to imaging spectrometer and lens, and $\square_2$ is the optical assembly flat image. The resulting $\square_1$ and $\square_2$ non-uniformity corrections are visualized in Figure 5. Note that both these corrections are essential in calibrating the camera and producing level 1 images.
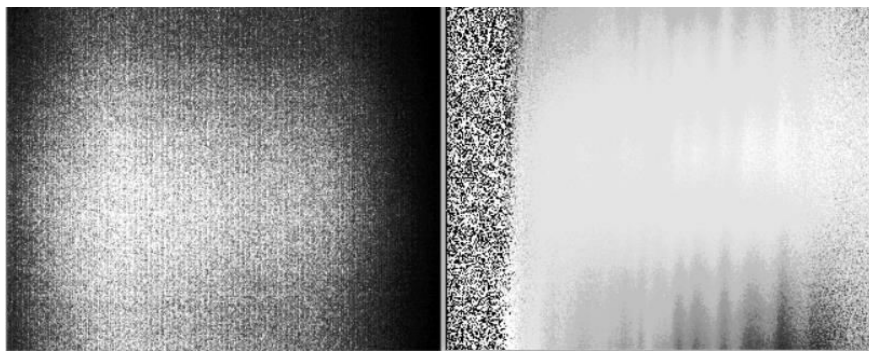

Figure 5. Flat-fielding images accounting for the USB camera (left) and imaging spectrometer with lens (right) non-uniformity.

3.2 Image quality characterization

The camera and lens system's image quality was characterized by calculating the modulation transfer function (MTF). With this, we could determine the lowest resolvable resolution that the system can measure.
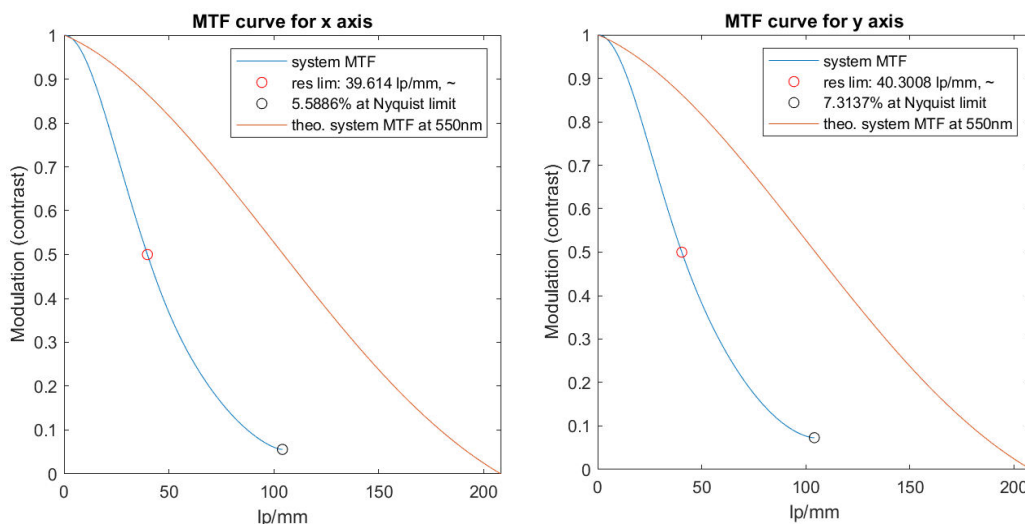

Figure 6. Modulation transfer function(MTF) of the imaging system for the x and y axes, plotted against the theoretical system MTF.

A slanted edge screen projection was captured using the system to determine the imaging resolution limit. Transects of the edge area near the image center were taken to get the edge spread function (ESF). The derivatives of the ESFs were computed to get the line spread function (LSF). The LSFs were Fourier

transformed to get the modulation transfer function (MTF). The spatial resolution that corresponds to 50% modulation (contrast) was taken to be the resolution limit (Burns & Williams, 1999). The system MTF is the product of the sensor MTF (defined by a sinc function dependent on the pixel width) and the lens MTF (dependent on the wavelength and f-number) (Hollows & James, (n.d.); Boreman, 2001).

Figure 6 shows the resolution limits for the two axes, with slight differences in value but both close to approximately 40 lp/mm, or 0.19 lp/px.

Discrepancies between axes and from the calculated theoretical system MTF can be primarily attributed to the lens design's aberration correction. Furthermore, slight misalignments in capture and errors from manufacturing deviations for the camera and lens system will decrease the experimentally measured MTF.

3.3 Imaging spectrometer characterization

The effect of the two main parts of the imaging spectrometer: (1) the slit and (2) the PGP dispersion element, was investigated. This section is divided into three parts to discuss the imaging spectrometer's effect on the recorded data's intensity, spectral, and spatial components.

Intensity characterization: Intensity measurements from varying slit widths, in this case, 50 and 80 μm, were compared to investigate its effect on the intensity throughput of the imaging spectrometer. Figure 7 shows the output dispersed wavelength components of the integrating sphere with the same radiant power measured by imaging spectrometers with 50 and 80 μm slits. It shows that a higher DN value was measured for the wider slit for the same light intensity. This is expected as the 80 μm slit allows more incoming light than the narrower 50 μm imaging spectrometer.
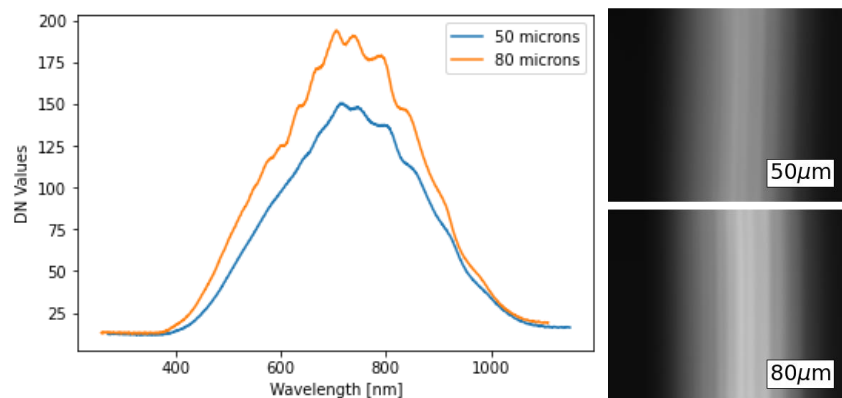

Figure 7. Comparison of DN value measurements by 50 and 80 μm payload prototypes. (Right) Actual images taken by the payload prototypes.

Aside from the slit width, the intensity throughput of the imaging spectrometer is also affected by the dispersive properties of the PGP component. According to the simulated transmission function provided by the manufacturer, the intensity decreases to 29%, 46%, and 36% for wavelengths of 400 nm, 550 nm, 700 nm (SPECIM Spectral Imaging Ltd., 2021). This is mainly due to the dispersion of the total energy into several diffraction orders, while the imaging spectrometer only captures a single-order spectrum.

Therefore, the imaging spectrometer affects the intensity in two ways: (1) by limiting the incoming light passing through the slit, and (2) by attenuating the energy due to dispersion to multiple orders.

Spectral characterization: To analyze the effect of the imaging spectrometer's slit on the spectral measurements, the discrete spectral bands of the Mercury emission lamp were captured using 50 and 80 μm slit imaging spectrometers. Shown in Figure 8 is the comparison between the spectral bandwidth of 50 and 80 μm slit width. It is evident that the spectral band width increases as the slit widens. Since the payload system can measure continuous spectrum, the spectral bands along the wavelength axis overlap. This increases the uncertainty in spectral measurement as slit width increases. For our payload system, the estimated uncertainty is ±3.475nm and ±5.56nm for 50 and 80 μm, respectively.
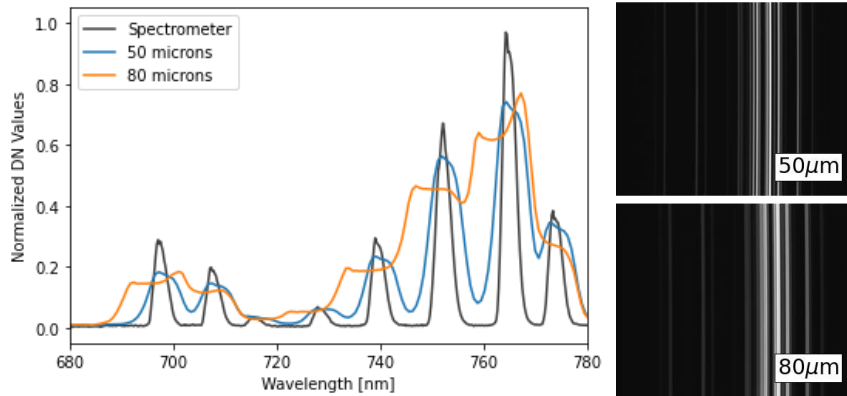
Figure 8. Mercury emission lamp spectrum measurements of the 50 and 80 microns slit width payload prototypes and a reference spectrometer measurement (Ocean Optics USB4000). It is noted that the difference in normalized amplitude is due to the difference in sensor sensitivity since both the spectrometer and payload prototypes were not yet radiometrically calibrated. (Right) Actual images taken by the payload prototypes.

Moreover, the slit effect on the resulting reflectance was also investigated in correspondence to the agricultural mission objectives of the developed payload system. Actual spectral measurements using an ASD spectrometer of a vegetation (leaf) and its illumination (sun) was used to simulate the effect of slit width on the spectrum of the target object, illumination, and the resulting reflectance. This was done by convolving the spectral measurements with the estimated bandwidth due to the slit's field of view. Shown in Figure 9 are the convolved sun, leaf spectrum, and calculated reflectance for 50, 80, and 150 μm slits. As observed, the sharp spectral details were lost as the slit width increased. However, the resulting reflectance for varying slit widths shows no deviation from the actual reflectance measured by a reference spectrometer. This shows that as long as the spectral bandwidth for both target and illumination spectrum is the same, the slit effect on reflectance spectrum is negligible.
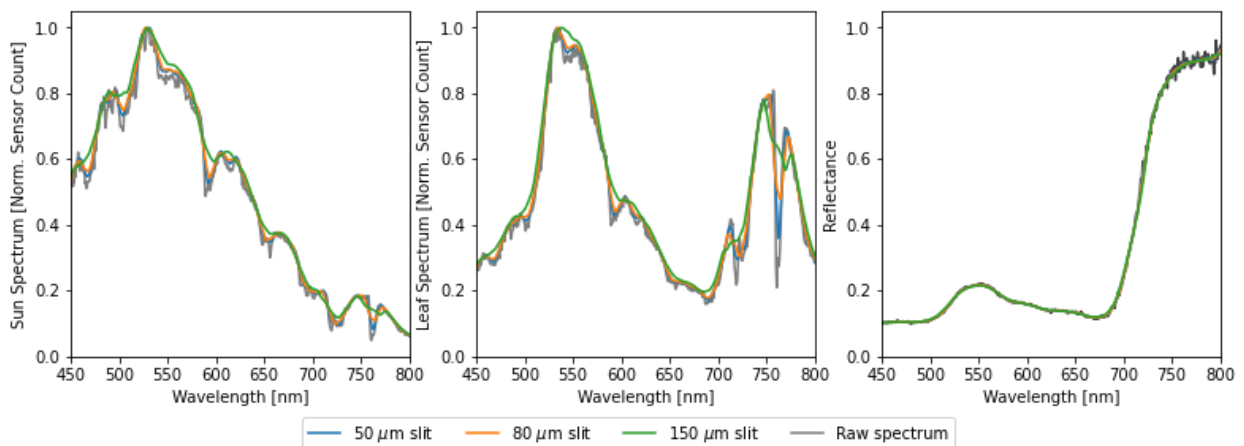

Figure 9. Simulated slit effect on actual spectral measurements

Spatial characterization: Lastly, the imaging spectrometer affects the quality of the 2D spatial information as the slit width affects the sharpness of the scanned image. It is noted that the spatial resolution of the scanned image is also dependent on the combination of camera parameters (frame rate and exposure time), and flight parameters (velocity), and their resulting overlapping frame. As discussed by Aguinaldo, et al. (2020), a shorter exposure time yields a sharper image while the optimal frame rate increases as velocity increases. Nonetheless, for the same camera and flight parameters, the slit width still determines the percentage of overlap between lines of captures for a scanned image, thus the image's sharpness. In order to visualize the effects, a blurring simulation was performed by convolution of the slit's field of view on an actual drone snapshot with a similar target ground sampling distance to the developed payload system.
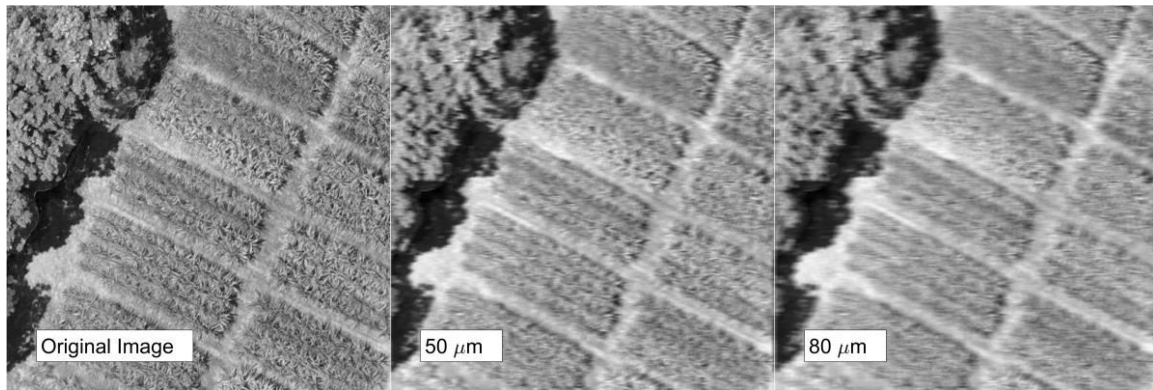
Figure 10. Simulated blurring due to slit effect on an actual drone image (green wavelength band).

Shown in Figure 10 is a sample image captured by a commercial drone camera for the green wavelength band. Assuming that the scanning direction is along the horizontal axis and a single wavelength plane from the hyperspectral data cube, a 1-dimensional convolution of the slit to the image line scan was conducted. The figure illustrates that a wider slit width tends to have lower resolution (blurrier), increasing the percentage of slit's field of view overlaps. We approximate the spatial resolution to be 42 cm and 67 cm for 50 μm and 80 μm slits, respectively, assuming that the camera and flight parameters yield a 4 cm ground sampling distance for both across and along-track axis.

3. SUMMARY

The optical characteristics of an airborne push-broom hyperspectral imager were presented and analyzed in this study. The sensor characterization shows that the dark noise is not a variable of exposure time but is proportional to the gain settings. At the same time, the camera DN values were found to be linear with respect to both exposure time and gain. The photon transfer curve and flatness of the field were also presented in the study. Moreover, the image quality analysis was performed by calculating the modulation transfer functions and showing that the camera and lens system can resolve up to 40 lp/mm, or 0.19 lp/px.

Lastly, the effects of the imaging spectrometer were discussed. It was shown that as we increase the slit width, the intensity throughput also increases. It was also noted that the imaging spectrometer attenuates the power mostly due to the dispersion properties of the optical components within the instrument. The simulation and actual data also showed that it affects the spectrum measurements by increasing the bandwidth and reducing resolved information as the slit width increases. Moreover, the spatial resolution along the scanning direction decreases as the slit width increases due to an increase in the overlapping slit's field of view given the same flight and camera parameters.

The characterization of the intrinsic properties of the in-house developed airborne push-broom hyperspectral imager is essential to produce high-quality and repeatable data for the mission application. For one, it is necessary for the corrections prior to radiometric calibration of the payload system to produce measurements in scientific units and be constant for different measurements. Moreover, with this information at hand, we will be able to design the field operations for the mission application more effectively, adapting to the system's capability and limitations.

ACKNOWLEDGEMENT

REFERENCES

Aasen, H., Honkavaara, E., Lucieer, A., & Zarco-Tejada, P. 2018. Quantitative Remote Sensing at Ultra-High Resolution with UAV Spectroscopy: A Review of Sensor Technology, Measurement Procedures, and Data Correction Workflows. Remote Sensing, 10(7), 1091.

Adão, T., Hruška, J., Pádua, L., Bessa, J., Peres, E., Morais, R., & Sousa, J. 2017. Hyperspectral Imaging: A Review on UAV-Based Sensors, Data Processing and Applications for Agriculture and Forestry. Remote Sensing, 9(11), 1110.

Aguinaldo, R. A. S., Lofamia, M. C. P., Maestro, M. A. M., Bañas, A. R. M., & Soriano, M. N. 2020. Modulation transfer function of a scanning hyperspectral imager. Proceedings of the Samahang Pisika ng Pilipinas 38, SPP-2020-3D-10-1.

Aikio, M. 2001. Hyperspectral Prism-grating-prism Imaging Spectrograph. Espoo, Finand: VTT Publications.
Barreto, M., Johansen, K., Angel, Y., & McCabe, M. 2019. Radiometric Assessment of a UAV-Based Push-Broom Hyperspectral Camera. Sensors, 19(21), 4699.

Boreman,G. D. 2001. Modulation Transfer Function in Optical and Electro-Optical Systems, SPIE Press, Bellingham, WA.

Burns, P. D., & Williams, D. 1999. Using Slanted Edge Analysis for Color Registration Measurement, 51–53. Proc. IS&T PICS 1999: IMAGE PROCESSING, IMAGE QUALITY, IMAGE CAPTURE, SYSTEMS CONFERENCE, Savannah, Georgia.

Hollows, G., & James, N. (n.d.). Resolution. Retrieved September 17, 2021, from https://www.edmundoptics.com/knowledge-center/application-notes/imaging/resolution/.

Hruska, R., Mitchell, J., Anderson, M., & Glenn, N. F. 2012. Radiometric and Geometric Analysis of Hyperspectral Imagery Acquired from an Unmanned Aerial Vehicle. Remote Sensing, 4(9), 2736–2752.

Janesick, J. R. 2007. DN to λ. Bellingham, Washington: SPIE.

Pagnutti, M., Ryan, R. E., Cazenavette, G., Gold, M., Harlan, R., Leggett, E., & Pagnutti, J. 2017. Laying the foundation to use Raspberry Pi 3 V2 camera module imagery for scientific and engineering purposes. Journal of Electronic Imaging, 26(1), 013014.

SPECIM Spectral Imaging Ltd. 2021. V10 Transmission.

Stuart, M. B., McGonigle, A. J. S., & Willmott, J. R. 2019. Hyperspectral Imaging in Environmental Monitoring: A Review of Recent Developments and Technological Advances in Compact Field Deployable Systems. Sensors, 19(14), 3071.